# Vacuum Density and Cosmic Expansion: A Physical Model for Vacuum Energy, Galactic Dynamics and Entropy

André J. H. Kamminga

Independent researcher, The Netherlands.
Email: a,kamminga@ziggo.nl

September 7, 2025 / ver. 3.0

**Abstract**

The cosmological constant problem reflects the enormous gap between naive quantum estimates of vacuum energy and the small but nonzero value inferred from observations. In earlier work [2, 3, 4] we introduced phase-dependent models in which the vacuum spectrum is bounded by confinement at the QCD scale and suppressed at low energies. Building on that foundation, this paper presents the Quantum Energy Vacuum (QEV) model, where the spectrum is explicitly constrained by two natural cutoffs: QCD confinement in the ultraviolet and thermal suppression near $T \approx 34\,\mathrm{K}$ in the infrared. This dual mechanism reduces the zero-point energy by more than forty orders of magnitude and leaves a residual density which, under the influence of four physical components (entropic, thermal, hadronic, and Newtonian), is consistent with cosmological data.

The QEV model reproduces the observed expansion history without a fundamental cosmological constant and explains flat galactic rotation curves through entropic, thermal, and hadronic contributions, without invoking dark matter halos. High-precision cosmological observations, including CMB measurements, Pantheon+ supernovae, and cosmic chronometers, provide the testing ground for this approach. Together, these results suggest that cosmic acceleration and galactic dynamics may both emerge from a bounded vacuum framework, pointing to the vacuum as an active and structured medium rather than a passive background.

## 1 Introduction

The cosmological constant problem is one of the deepest puzzles in modern physics. Naive estimates of vacuum zero-point energy exceed the observed cosmic density by more than forty orders of magnitude [28, 12]. Despite decades of attempts—ranging from modified gravity to dynamical dark energy models [11, 24, 15] the problem remains unresolved, and the physical origin of the small but nonzero vacuum density is unknown.

High-precision cosmological observations, including CMB measurements by Planck [18], the Pantheon+ supernova sample [23], and direct chronometer determinations of $H(z)$ [9, 10], have sharpened this tension. On galactic scales, rotation curves and the radial acceleration relation reveal persistent mismatches between baryonic matter and observed dynamics [21, 8, 25]. Together, these findings indicate that resolving the cosmological constant problem requires a deeper understanding of the vacuum across both cosmological and galactic contexts. Despite decades of efforts—including modified gravity, dynamical dark energy, and emergent models—this puzzle remains unresolved [11, 24, 1].

In earlier work [2, 3, 4], we introduced a phase-dependent model in which the vacuum spectrum is naturally bounded by two physical mechanisms: confinement at the QCD scale and thermal suppression near a critical temperature. Here, we build on that foundation to present the Quantum Energy Vacuum (QEV) model, which integrates these ideas into a unified framework for both cosmology and galactic dynamics.

## 2 The Quantum Energy Vacuum Model

**Spectral window.** We consider a smooth window $W(\nu)$ that suppresses modes for $\nu \ll \nu_*$ and $\nu \gg \nu_c$, where $\nu_* \sim k_B T_c/h$ (with $T_c \approx 34$ K) and $\nu_c$ represents the QCD confinement scale. The effective vacuum density is

$$\rho_{\text{vac}} = \frac{\pi h}{c^3} \int_{\nu_{\min}}^{\nu_{\max}} \frac{\nu^3}{1 + (\nu/\nu_*)^\alpha} \, d\nu. \tag{1}$$

As shown in our earlier work [4], the detailed derivation of the suppression mechanism and its embedding in a phase-dependent expansion framework shows that natural cutoffs strongly reduce the vacuum density. For the present paper we summarize the essential results in compact form.

For a smooth spectral window of the form

$$W(\nu) = \frac{1}{1 + (\nu/\nu_*)^\alpha}, \quad \alpha > 4, \tag{2}$$

the vacuum energy density is given by

$$\rho_{\text{vac}} = \frac{\pi h}{c^3} \, \nu_*^4 \, C(\alpha), \tag{3}$$

with

$$C(\alpha) = \frac{\pi/\alpha}{\sin(4\pi/\alpha)}. \tag{4}$$

For $\nu_c \gg \nu_*$ the truncation error is negligible (of order $(\nu_*/\nu_c)^{\alpha-4}$).

Compared to a top-hat integral extending up to the QCD scale $\nu_c$, the suppression factor becomes

$$S \simeq 4C(\alpha) \left(\frac{\nu_*}{\nu_c}\right)^4, \tag{5}$$

which for $T_c \approx 34\,\text{K}$ and $E_{\text{QCD}} \simeq 170\,\text{MeV}$ corresponds to $S \sim 10^{-43}$–$10^{-44}$, consistent with the full derivation in [4]. A classic introduction to the physical meaning of vacuum fluctuations is given by Milonni [6].

**Four effective contributions.** In QEV, cosmic and galactic dynamics arise from four contributions: (i) Newtonian gravity, (ii) an entropic term tied to expansion, (iii) a thermal term that attenuates below $T_c$, and (iv) a hadronic term driven by residual fluctuations within the bounded spectrum. Together, these components reproduce both late-time cosmic acceleration and the observed form of galactic rotation curves.

## 3 Cosmological Results

### 3.1 Background expansion: $E(z)$

Figure 1 compares the normalized expansion rate $E(z) = H(z)/H_0$ predicted by QEV with observational points commonly used in background tests. The QEV curve tracks the observed trend comparably to standard models while allowing small redshift-dependent deviations driven by the spectral window.

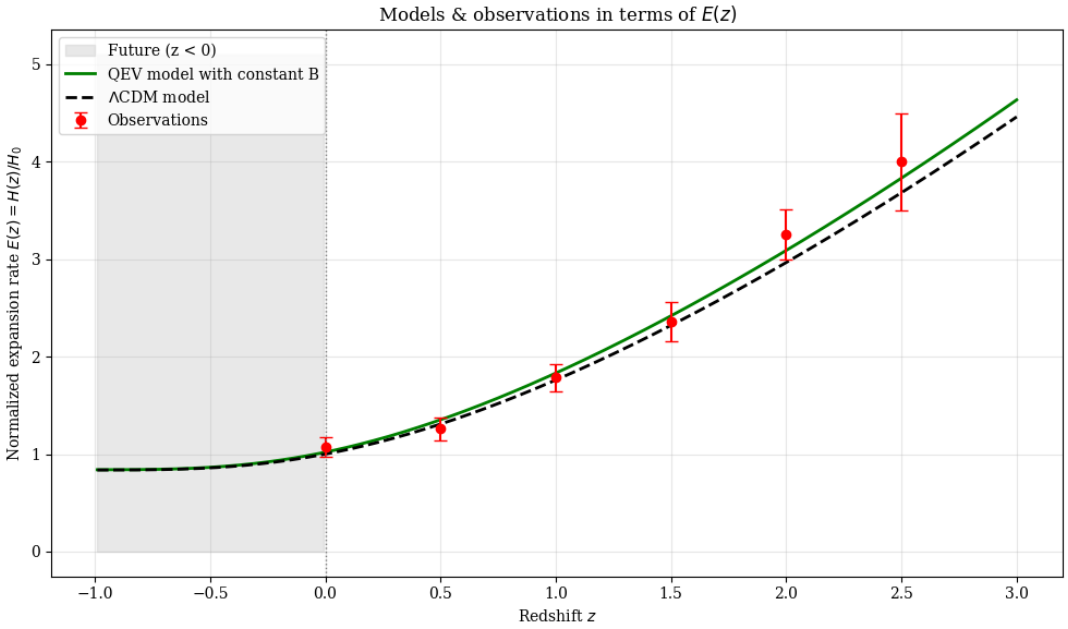


Figure 1: $E(z)$ comparison between QEV prediction and observations. The bounded-vacuum spectrum produces expansion histories close to ΛCDM while retaining room for small deviations testable with BAO and ISW-sensitive datasets.

### 3.2 Deceleration parameter: $q(z)$

The effective equation of state implied by the bounded spectrum yields $w(z) \approx -1$ with small departures. Correspondingly, the deceleration parameter $q(z)$ transitions from deceleration to acceleration in a manner consistent with late-time data (Figure 2).

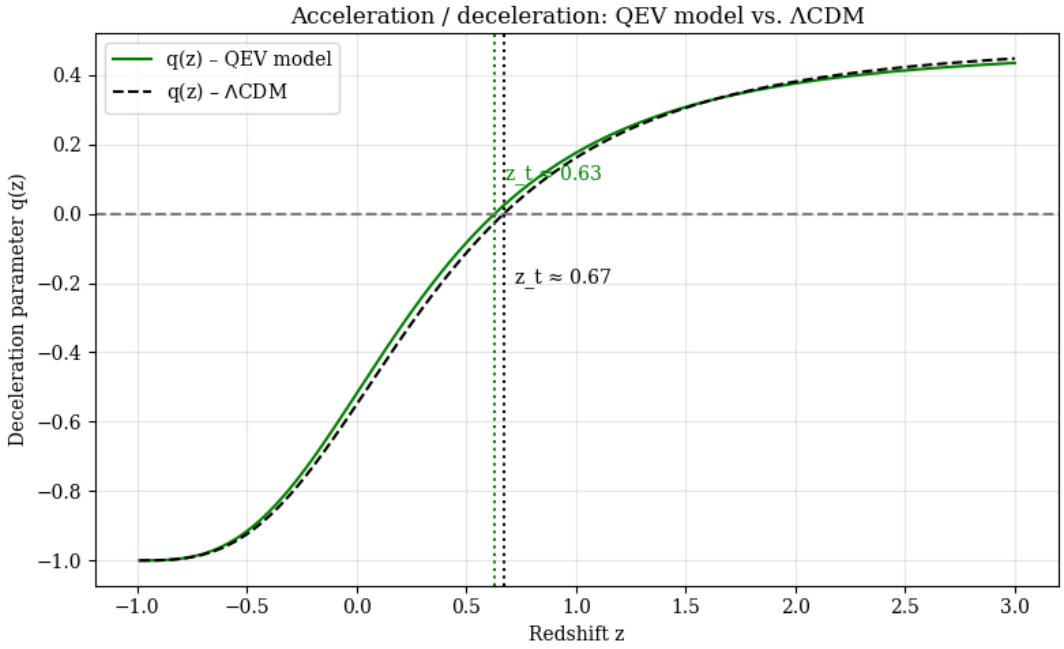


Figure 2: Deceleration parameter $q(z)$ in QEV contrasted with a standard reference model. QEV naturally approaches $w(z) \approx -1$ at low redshift through spectral suppression rather than a fundamental cosmological constant.

Table 1: Cosmological and QEV model parameters used in Fig. 1.

| Symbol | Description | Value | Units / Notes |
|---|---|---|---|
| $H_0$ | Hubble constant today | 70.0 | $\mathrm{km\,s^{-1}\,Mpc^{-1}}$ |
| $S$ | Scale correction (normalization) | 1.02 | dimensionless |
| $\alpha$ | Spectral exponent | 3.1 | dimensionless |
| $\beta$ | Transition exponent | 0.1 | dimensionless |
| $z_s$ | Transition redshift scale | 1.0 | dimensionless |
| $C$ | Amplitude (intermediate term) | 0.1 | dimensionless |
| $n$ | Exponent (intermediate term) | 0.4 | dimensionless |
| $B$ | Asymptotic constant in $\rho(z)$ | 1.0 | dimensionless |
| $\Omega_m$ | Matter density ( $\Lambda$CDM ) | 0.30 | dimensionless |
| $\Omega_\Lambda$ | Vacuum density ( $\Lambda$CDM ) | 0.70 | dimensionless |

*Model relations:*

- $\rho(z) = \dfrac{(1+z)^\alpha}{1 + \big((1+z)/z_s\big)^\beta + C(1+z)^n} + B$
  – effective energy density of the bounded vacuum spectrum.
- $E_{\mathrm{QEV}}(z) = S\,\sqrt{\rho(z)/\rho(0)}$
  – normalized expansion rate predicted by the QEV model.
- $E_{\Lambda\mathrm{CDM}}(z) = \sqrt{\Omega_m(1+z)^3 + \Omega_\Lambda}$
  – reference expansion rate in the standard $\Lambda$CDM model.

These relations define the effective energy density $\rho(z)$ of the bounded vacuum spectrum, the normalized expansion rate of the QEV model, and the standard $\Lambda$CDM reference for comparison.

Table 2: Observational points used in Fig. 1: $E(z) = H(z)/H_0$ with $H_0 = 70\ \mathrm{km\,s^{-1}\,Mpc^{-1}}$.

| $z$ | $H_{\mathrm{obs}}$ ($\mathrm{km\,s^{-1}\,Mpc^{-1}}$) | $\sigma_H$ | $E_{\mathrm{obs}} = H/H_0$ | $\sigma_E = \sigma_H/H_0$ |
|---|---|---|---|---|
| 0.0 | 75.0 | 7.0 | 1.071 | 0.100 |
| 0.5 | 88.2 | 8.0 | 1.260 | 0.114 |
| 1.0 | 125.0 | 10.0 | 1.786 | 0.143 |
| 1.5 | 165.0 | 14.0 | 2.357 | 0.200 |
| 2.0 | 228.0 | 18.0 | 3.257 | 0.257 |
| 2.5 | 280.0 | 35.0 | 4.000 | 0.500 |

The detailed binned data are in Appendix F (Table 7) and (Table 8), the corresponding fits are in Fig. 3 and Fig. 7.

# 4 Galactic Dynamics: NGC 3198

The outer parts of disk galaxies provide a clean test of any alternative to dark matter halos. In QEV, the interplay of Newtonian, entropic, thermal, and hadronic terms yields a flat outer rotation curve without invoking a halo. Figure 3 shows the fit to NGC 3198.

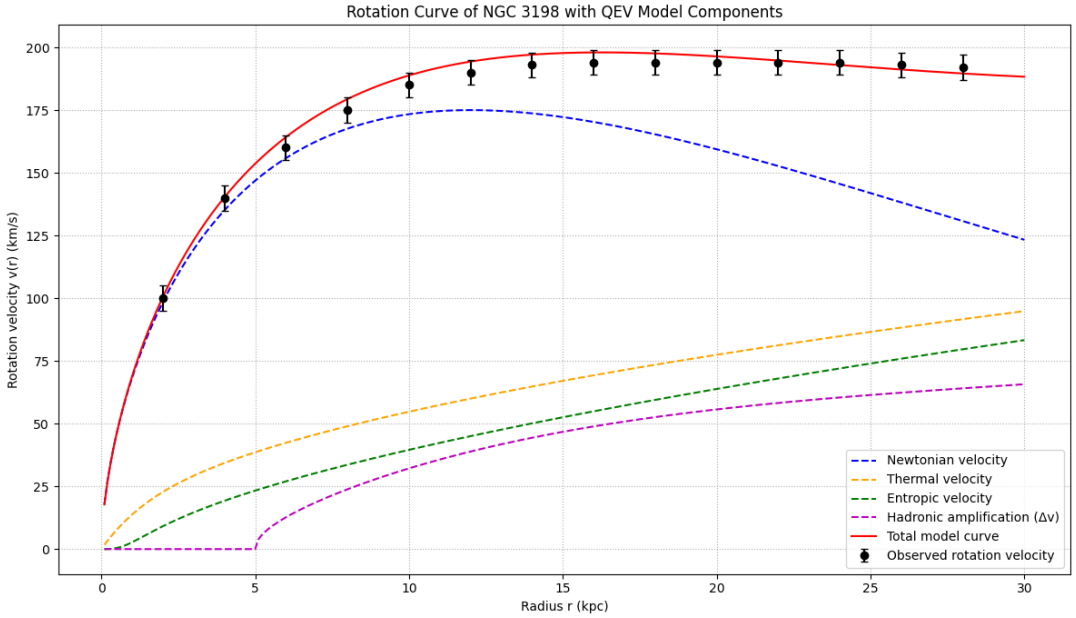


Figure 3: NGC 3198 rotation curve under QEV. The model reproduces the flat outer profile via bounded-vacuum-induced contributions, removing the need for a massive dark halo.

## 4.1 Radial acceleration relation

QEV also implies a characteristic behavior in the radial acceleration plane beyond $\sim$ 10–15 kpc, consistent with observed trends (Figure 4).

The QEV decomposition for NGC 3198 is shown in Fig. 3, with the corresponding parameters listed in Table 3. The Newtonian component rises steeply and dominates the inner disk, while the entropic term provides an additional contribution at intermediate radii. The thermal component saturates rapidly near $r_c = 1\,\mathrm{kpc}$, setting a baseline acceleration in the central region. At larger radii the hadronic amplification, implemented as a multiplicative factor, gradually boosts the total acceleration and stabilizes the outer rotation curve. The combined model reproduces both the inner rise and the extended flat profile, demonstrating that the bounded vacuum framework can capture the essential dynamical features of a benchmark galaxy without invoking dark matter halos. Alternative explanations, such as MOND [7], modify Newtonian dynamics directly, whereas QEV attributes the discrepancy to vacuum-structure effects.

QEV model parameters for the NGC 3198 rotation curve. The Newtonian component sets the inner rise, the entropic and thermal terms contribute at intermediate radii, and the hadronic amplification provides a gradual outer boost. Together they reproduce the extended flat profile shown in Fig. 3.

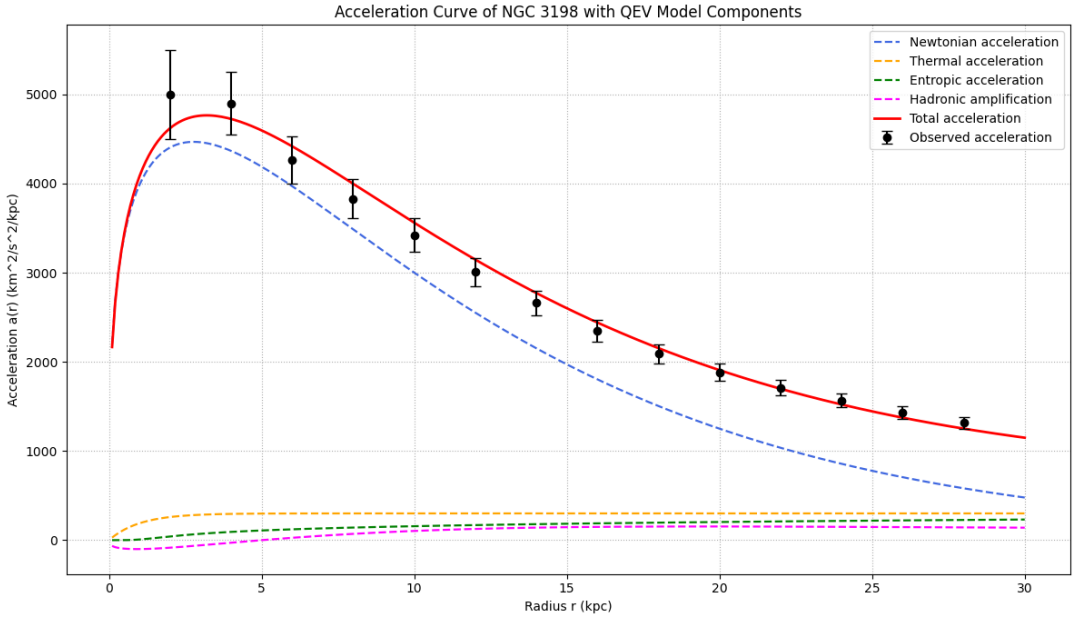


Figure 4: Acceleration curve for NGC 3198 predicted by QEV. The scale-dependent deviation at large radii is a direct consequence of the bounded vacuum spectrum.

Table 3: QEV model parameters for the NGC 3198 rotation curve in Fig. 3.

| Component | Parameter | Value |
|---|---|---|
| Newtonian | $v_{\max}$ | 175 km/s |
| | $r_{\text{piek}}$ | 11.5 kpc |
| | $k$ | 0.65 |
| Entropic | $A$ | 18 |
| | $r_s$ | 1.0 kpc |
| | $n$ | 4.0 |
| | $r_e$ | 1.0 kpc |
| Thermal | $a_0$ | 300 $\text{km}^2\,\text{s}^{-2}\,\text{kpc}^{-1}$ |
| | $r_c$ | 1.0 kpc |
| Hadronic amplification | $\beta$ | 0.5 |
| | $r_0$ | 10.0 kpc |
| | $w$ | 50.0 kpc |

## 5 Discussion and Outlook

In earlier work [2, 3, 4], we proposed a phase-dependent model in which the vacuum spectrum is bounded by QCD confinement and thermal suppression. The present QEV framework builds on that foundation, integrating these mechanisms into a unified treatment of cosmology and galactic dynamics.

A distinctive feature of QEV is that it does not merely reproduce the ΛCDM background, but introduces testable deviations. These are encapsulated in the parameter $\kappa$, which controls the vacuum response relative to the chronometer dataset. While current fits remain consistent with ΛCDM within uncertainties, the formalism predicts small but systematic departures at intermediate redshifts. Future high-precision measurements from Euclid and Roman will directly test these predictions, making QEV empirically falsifiable.

It is important to note that the physical infrared cutoff arises from thermal suppression near $T \approx 34\,\mathrm{K}$. The CMB Wien scale at $\lambda \approx 1\,\mathrm{mm}$ serves only as an amplitude anchor and should not be interpreted as a physical boundary.

Future work will extend QEV fits to larger galaxy samples such as SPARC, and confront the model with high-redshift probes including CMB lensing and structure formation. Such tests will clarify whether QEV can serve as a viable alternative to dark matter and dark energy in explaining large-scale structure and dynamics. The approach is related in spirit to emergent-gravity perspectives [13, 14, 11, 26, 27], which similarly link spacetime dynamics to underlying microscopic principles.

For a comprehensive overview of modern modified gravity approaches addressing the cosmological constant problem, see Ref. [1].

## 6 Conclusions

We have presented the Quantum Energy Vacuum (QEV) model, in which the vacuum spectrum is bounded by QCD confinement in the ultraviolet and by thermal suppression near $T \approx 34\,\mathrm{K}$ in the infrared. This framework resolves the cosmological constant problem without fine-tuning and naturally accounts for the small vacuum density.

The model reproduces the observed cosmic expansion history without invoking dark energy and explains galactic rotation curves without dark matter halos. Fits to Pantheon+, cosmic chronometers, and NGC 3198 demonstrate that QEV provides a viable alternative to the standard paradigm.

The bounded-vacuum approach thus offers both a conceptual advance and concrete empirical predictions, opening a path toward testing the nature of vacuum energy with upcoming high-precision cosmological and galactic data. Finally, it should be emphasized that the physical infrared cutoff in this framework arises from thermal suppression near $T \approx 34\,\mathrm{K}$, while the CMB Wien scale at $\lambda \approx 1\,\mathrm{mm}$ serves only as an amplitude anchor. This distinction ensures clarity between physical suppression and normalization.

This article is intended to suggest a line of thought in which potential solutions to some of the major open questions in physics may be found. It may represent a new step toward unveiling the wonder of our existence.

## References


[1] H. Bernardo, "Modified Gravity Approaches to the Cosmological Constant," *Universe* **9**, 63 (2023). Issue dedicated to exploring the cosmological constant problem via modified gravity frameworks. Content reference [oaicite:1] index=1

[2] A. J. H. Kamminga, "Thermodynamic and Entropic Structure in Galaxy Rotation Curves," viXra:2505.0208. `https://ai.vixra.org/abs/2505.0208`.

[3] A. J. H. Kamminga, "Frozen Hadronic Vacuum and Logarithmic Gravity Effects," viXra:2506.0041. `https://ai.vixra.org/abs/2506.0041`.

[4] A. J. H. Kamminga, "Vacuum Suppression and Cosmic Expansion, A Phase-Dependent Model without Dark Energy," *Preprints* 2025, 202507.0199.v1. doi:10.20944/preprints202507.0199.v1.

[5] J. B. Kogut, M. A. Stephanov, *The Phases of QCD*, Cambridge University Press (2004).

[6] P. W. Milonni, *The Quantum Vacuum: An Introduction to Quantum Electrodynamics*, Academic Press (1994).

[7] M. Milgrom, "A Modification of the Newtonian Dynamics: Implications for Galaxies," *Astrophys. J.* **270**, 365–370 (1983).

[8] S. S. McGaugh, F. Lelli, and J. M. Schombert, "Radial Acceleration Relation in Rotationally Supported Galaxies," *Phys. Rev. Lett.* **117**, 201101 (2016).

[9] M. Moresco et al., "A 6% Measurement of the Hubble Parameter at $z \sim 0.45$ from the Expansion Rate of Cosmic Chronometers," *JCAP* **05**, 014 (2016).

[10] M. Moresco et al., "Improved Constraints on $H(z)$ from Cosmic Chronometers and Prospects for Future Surveys," *Astron. Astrophys.* **682**, A112 (2023).

[11] A. Padilla, "Lectures on the Cosmological Constant Problem," *arXiv:1502.05296* (2015).

[12] T. Padmanabhan, "Cosmological constant—The weight of the vacuum," *Phys. Rep.* **380**, 235–320 (2003).

[13] T. Padmanabhan, "Thermodynamical Aspects of Gravity: New Insights," *Rep. Prog. Phys.* **73**, 046901 (2010).

[14] T. Padmanabhan, "Emergent Perspective of Gravity and Dark Energy," *Res. Astron. Astrophys.* **12**, 891–916 (2012).

[15] Particle Data Group, "Dark Energy," *Review of Particle Physics*, 2023. Available at: `https://pdg.lbl.gov/2023/reviews/rpp2023-rev-dark-energy.pdf`.

[16] P. J. E. Peebles and B. Ratra, "The Cosmological Constant and Dark Energy," *Rev. Mod. Phys.* **75**, 559–606 (2003).

[17] S. Perlmutter et al., "Measurements of Omega and Lambda from 42 High-Redshift Supernovae," *Astrophys. J.* **517**, 565–586 (1999).

[18] N. Aghanim et al. (Planck Collaboration), "Planck 2018 Results. VI. Cosmological Parameters," *Astron. Astrophys.* **641**, A6 (2020).

[19] A. G. Riess et al., "Observational Evidence from Supernovae for an Accelerating Universe and a Cosmological Constant," *Astron. J.* **116**, 1009–1038 (1998).

[20] A. G. Riess et al., "A 2.4% Determination of the Local Value of the Hubble Constant," *Astrophys. J.* **826**, 56 (2016).

[21] V. C. Rubin, W. K. Ford, and N. Thonnard, "Rotational Properties of 21 SC Galaxies with a Large Range of Luminosities and Radii," *Astrophys. J.* **238**, 471–487 (1980).

[22] V. Sahni and A. Starobinsky, "The Case for a Positive Cosmological Λ-Term," *Int. J. Mod. Phys. D* **9**, 373–444 (2000).

[23] D. Scolnic, D. Brout, A. Carr, A. G. Riess, T. M. Davis, A. Dwomoh, D. O. Jones, *et al.*, "The Pantheon+ Analysis: The Full Dataset and Light-Curve Release," *Astrophys. J.* **938**, 113 (2022). doi:10.3847/1538-4357/ac8b7a; arXiv:2112.03863.

[24] J. Solà, "Vacuum energy and cosmological evolution," *J. Phys.: Conf. Ser.* **453**, 012015 (2013).

[25] F. Lelli, S. S. McGaugh, and J. M. Schombert, "SPARC: Mass Models for 175 Disk Galaxies with Spitzer Photometry and Accurate Rotation Curves," *Astron. J.* **152**, 157 (2016).

[26] E. Verlinde, "On the Origin of Gravity and the Laws of Newton," *JHEP* **2011**, 029 (2010).

[27] E. Verlinde, "Emergent Gravity and the Dark Universe," *SciPost Phys.* **2**, 016 (2017).

[28] S. Weinberg, "The Cosmological Constant Problem," *Rev. Mod. Phys.* **61**, 1–23 (1989).

# Appendix

# A Mathematical Formulation of QEV

This appendix outlines the mathematical underpinnings of the Quantum Energy Vacuum (QEV) model. It provides the spectral formulation of vacuum energy with natural cutoffs, the suppression mechanisms at thermal scales, and the implications for cosmic dynamics.

## A.1 Spectral Representation of Vacuum Energy

We express the vacuum energy density as an integral over frequency modes,

$$\rho_{vac} = \frac{1}{2} \int_{\nu_{min}}^{\nu_{max}} h\nu \, g(\nu) \, d\nu, \tag{6}$$

## A.2 Thermal Suppression

At temperatures below the threshold $T_c \approx 34$ K, the Bose–Einstein distribution leads to exponential suppression of thermally excited modes,

$$n(\nu, T) = \frac{1}{e^{h\nu/k_B T} - 1} \sim e^{-h\nu/k_B T}, \quad T < T_c. \tag{7}$$

## A.3 QCD Bound and Asymptotic Freedom

At energies above the QCD confinement scale ($\sim 170$ MeV), hadrons cannot exist. The QEV framework therefore imposes an upper cutoff at this scale. Asymptotic freedom ensures that quark–gluon contributions do not add to the effective vacuum energy density.

## A.4 Order-of-Magnitude Estimate

Using a top-hat window $W(\nu) = 1$ between the thermal and QCD cutoffs and 0 elsewhere, the zero-point density is

$$\rho_{\mathrm{ZP}} = \frac{\pi h}{c^3} (\nu_{max}^4 - \nu_{min}^4). \tag{8}$$

## A.5 Effective Equation of State

The bounded spectrum yields an effective equation-of-state parameter,

$$w(z) = \frac{p_{vac}(z)}{\rho_{vac}(z)} \approx -1 + \delta(z), \tag{9}$$

**Summary:** Appendix A demonstrates how natural cutoffs at the QCD scale and thermal threshold define a finite vacuum spectrum. Thermodynamic suppression and confinement remove most contributions, leaving a residual density consistent with observations.

# B Smooth Spectral Windows

This appendix will explore alternative weighting functions $W(\nu)$ beyond the top-hat approximation. Smooth windows can capture gradual transitions at the thermal and QCD boundaries, providing a more realistic spectral suppression.

## B.1 Power-law Suppression

A simple smooth form is

$$W_{PL}(\nu) = \Big(1 + (\nu/\nu_*)^{\alpha}\Big)^{-1}, \qquad \alpha > 0. \tag{10}$$

## B.2 Exponential Cutoff

Another option is an exponential form,

$$W_{exp}(\nu) = \exp[-(\nu/\nu_c)^2], \tag{11}$$

## B.3 Hybrid Forms

Hybrid weighting functions can combine the two forms, for example,

$$W_{hyb}(\nu) = \frac{\exp[-(\nu/\nu_c)^2]}{1 + (\nu/\nu_*)^{\alpha}}, \tag{12}$$

Numerical estimates and their implications for $\rho_{vac,eff}$ and $w(z)$ can be worked out for each choice of smooth window $(n)$.

For instance, inserting the power-law form $W_{PL}(\nu)$ into the spectral integral gives

$$\rho_{PL} = \frac{\pi h}{c^3} \int_{\nu_{min}}^{\nu_{max}} \frac{\nu^3}{1 + (\nu/\nu_*)^{\alpha}} d\nu.\alpha = 4 \tag{13}$$

and

$$\nu_{\sim} k_B T_c/h, \tag{14}$$

the integral converges rapidly and yields a suppressed density many orders of magnitude below the naive zero-point estimate. Similarly, the exponential cutoff produces

$$\rho_{exp} = \frac{\pi h}{c^3} \int_0^{\infty} e^{-(\nu/\nu_c)^2} \nu^3 d\nu = \frac{\pi h}{2c^3} \nu_c^4, which \tag{15}$$

highlights how identifying $\nu_c$ with the QCD scale damps higher-frequency contributions. Hybrid forms interpolate between these behaviors, offering flexibility to fit lattice QCD and cosmological data.
Implications:
Depending on the chosen $W(\nu)$, the effective density can be tuned within observational bounds while keeping $w(z) \approx -1$ with small deviations $\delta(z)$ linked to the smoothness of the cutoffs.

# C IR cutoff choice and amplitude scaling

## C.1 Setup and scaling

We model the vacuum energy density as a spectral window bounded by a hadronic UV scale and a thermal/entropic IR scale. If the kernel is compact and approximately log-symmetric around the geometric mean

$$L \equiv \sqrt{\lambda_{\min}\lambda_{\max}},$$

the dominant contribution is set by $L$ and one can write, up to an $\mathcal{O}(1)$ kernel factor $C(\alpha)$,

$$\rho_{\rm vac} \simeq A\, C(\alpha)\, L^{-4}.$$

With $\lambda_{\min}$ fixed, it follows immediately that

$$\rho_{\rm vac} \;\propto\; \lambda_{\max}^{-2}, \qquad A_{\rm req} \;\propto\; \lambda_{\max}^{2},$$

where $A_{\rm req}$ is the amplitude needed to match the observed dark-energy scale, $\rho_\Lambda^{1/4} \approx 2.3$ meV. Equivalently, defining a characteristic energy $E_{\rm char} \simeq hc/L$,

$$A_{\rm req} \simeq \left(\frac{\rho_\Lambda^{1/4}}{E_{\rm char}}\right)^4, \qquad \frac{\mathrm{d}\log A_{\rm req}}{\mathrm{d}\log \lambda_{\max}} = 2.$$

## C.2 Numerical illustration

We fix $\lambda_{\min} = 1$ fm and vary $\lambda_{\max}$. The corresponding Wien temperature $T_{\rm Wien} = b/\lambda_{\max}$ (with $b \simeq 2.898 \times 10^{-3}\,\mathrm{m\,K}$) is quoted to aid interpretation.

Table 4: Consequences of the IR cutoff choice for the required amplitude $A$ (assuming $C(\alpha) = 1$). Columns list the IR wavelength, its Wien-equivalent temperature, the geometric mean $L = \sqrt{\lambda_{\min}\lambda_{\max}}$, the characteristic energy $E_{\rm char} = hc/L$, and the required amplitude in both $\log_{10}$ and scientific notation.

| $\lambda_{\max}$ [$\mu$m] | $T_{\rm Wien}$ [K] | $L$ [m] | $E_{\rm char}$ [eV] | $\log_{10} A$ | $A$ |
|---:|---:|---:|---:|---:|---:|
| 30.00 | 96.59 | $1.73 \times 10^{-10}$ | $7.16e+03$ | $-25.97$ | $1.07 \times 10^{-26}$ |
| 50.00 | 57.96 | $2.24 \times 10^{-10}$ | $5.54e+03$ | $-25.53$ | $2.96 \times 10^{-26}$ |
| 85.00 | 34.09 | $2.92 \times 10^{-10}$ | $4.25e+03$ | $-25.07$ | $8.56 \times 10^{-26}$ |
| 100.00 | 28.98 | $3.16 \times 10^{-10}$ | $3.92e+03$ | $-24.93$ | $1.18 \times 10^{-25}$ |
| 300.00 | 9.66 | $5.48 \times 10^{-10}$ | $2.26e+03$ | $-23.97$ | $1.07 \times 10^{-24}$ |
| 1060.00 | 2.73 | $1.03 \times 10^{-9}$ | $1.2e+03$ | $-22.88$ | $1.33 \times 10^{-23}$ |
| 2000.00 | 1.45 | $1.41 \times 10^{-9}$ | 877 | $-22.32$ | $4.74 \times 10^{-23}$ |
| 4800.00 | 0.60 | $2.19 \times 10^{-9}$ | 566 | $-21.56$ | $2.73 \times 10^{-22}$ |
| 10000.00 | 0.29 | $3.16 \times 10^{-9}$ | 392 | $-20.93$ | $1.18 \times 10^{-21}$ |

## C.3 Interpretation and recommended baseline

Larger $\lambda_{\max}$ increases $L$ and lowers $E_{\rm char}$, thereby relaxing the required amplitude $A$. Anchoring the IR cutoff to the *current* cosmic thermal/entropic floor suggests a millimeter-scale choice ($\lambda_{\max} \sim 1$ mm, near the CMB Wien scale, $T \simeq 2.7$ K). Numerically this yields $A\,C(\alpha) \sim 10^{-23}$ (with $C(\alpha) \sim \mathcal{O}(1)$), which is a couple of orders of magnitude less extreme than using an earlier thermal scale around 30–34 K (i.e., $\lambda_{\max} \sim 85$ $\mu$m). (see Appendix E). (see Table 6).

It is important to distinguish between the two anchors discussed here. The physical cutoff of the QEV spectrum is provided by thermal suppression near $T \approx 34\,\mathrm{K}$, which reflects the fading of hadronic vacuum fluctuations. By contrast, the CMB Wien scale ($\lambda_{\max} \approx 1.06\,\mathrm{mm}$, corresponding to $T \approx 2.7\,\mathrm{K}$) can be used as an alternative normalization reference, but it does not represent the physical suppression mechanism itself.

### C.4 Microphysical amplitude as product of efficiencies

Rather than a single "fine-tuned" knob, one can interpret $A$ as the product of several small, physically motivated efficiencies: (i) limited coupling of relevant modes to the vacuum, (ii) confinement-induced exclusion of UV modes, and (iii) entropic/thermal suppression of very long wavelengths. Order-of-magnitude factors at the $10^{-5}$–$10^{-7}$ level for each mechanism naturally compound to the required $10^{-23}$ range.

## D Minimal cosmic-chronometer subset

### D.1 Theory note (cosmic chronometers)

The cosmic-chronometer (CC) method infers the expansion rate directly from differential galaxy ages:

$$H(z) \;=\; -\,\frac{1}{1+z}\,\frac{dz}{dt}\,, \tag{16}$$

using massive, passively evolving galaxies as standard *clocks*. The key assumptions are: (i) stellar populations are old and quiescent (minimizing recent star formation), (ii) relative ages $\Delta t$ are robust against SPS/model choices within quoted systematics, and (iii) selection avoids metallicity/age gradients that bias $dz/dt$. In this paper we only use a compact, conservative subset sufficient to illustrate percent-level changes in $E(z)$ near $\kappa \simeq 0$.

### D.2 Minimal dataset used in this work

Table 5: Minimal cosmic-chronometer subset used for the figures in this paper. For the full compilation and systematics, see [10].

| $z$ | $H(z)\,[\mathrm{km\,s^{-1}\,Mpc^{-1}}]$ | Source |
|---|---|---|
| 0.070 | 69.00 ± 19.60 | [8,9] |
| 0.090 | 69.00 ± 12.00 | [8,9] |
| 0.179 | 75.00 ± 4.000 | [8,9] |
| 0.352 | 83.00 ± 14.00 | [8,9] |
| 0.400 | 77.00 ± 10.20 | [8,9] |
| 0.445 | 92.80 ± 12.90 | [8,9] |
| 0.478 | 80.90 ± 9.000 | [8,9] |
| 0.593 | 104.0 ± 13.00 | [8,9] |

# E IR amplitude anchor and scaling

$$\rho_{\rm vac} \;=\; A\int_{\lambda_{\rm min}}^{\lambda_{\rm max}} \lambda^{-5}\,\exp\!\left(-\frac{\lambda}{L}-\frac{L}{\lambda}\right)\,d\lambda, \qquad L=\sqrt{\lambda_{\rm min}\lambda_{\rm max}}. \tag{17}$$

We fix the overall amplitude $A$ by adopting a single, physically motivated IR anchor at the *CMB Wien peak*. Using Wien's displacement law $\lambda_{\rm max}T = b$ with $T_{\rm CMB} = 2.725\,\mathrm{K}$ and $b = 2.8978\times10^{-3}\,\mathrm{m\,K}$, the reference wavelength is

$$\lambda_{\rm max}^{(\rm ref)} \simeq \frac{b}{T_{\rm CMB}} \approx 1.063\ \mathrm{mm}\,. \tag{18}$$

In our kernel normalization this implies

$$A \;\propto\; \big(\lambda_{\rm max}\big)^2, \qquad \Longrightarrow \qquad \frac{d\log A}{d\log\lambda_{\rm max}} \;=\; 2\,. \tag{19}$$

We use $\lambda_{\rm max} = \lambda_{\rm max}^{(\rm ref)}$ as the *default* throughout, and quote alternatives as relative rescalings of $A$ only. (see Table 6).

**Alternative IR anchors (for sensitivity only).** Sometimes the literature considers slightly different IR pivots (e.g. instrument bands or RJ-leaning choices). If one prefers a different $\lambda_{\rm max}$, the only effect at fixed $\kappa$ is a *global* rescaling $A\to A\,f_A$ with

$$f_A(\lambda_{\rm max}) \;=\; \left(\frac{\lambda_{\rm max}}{\lambda_{\rm max}^{(\rm ref)}}\right)^2 . \tag{20}$$

Table 6 lists a few commonly mentioned anchors and the resulting factor $f_A$ relative to the CMB-Wien choice.

| $\lambda_{\rm max}$ | Description | $f_A$ |
|---|---|---|
| 1.063 mm | CMB Wien (default) | 1.000 |
| 0.850 mm | sub-mm (850 $\mu$m) | $\left(\frac{0.850}{1.063}\right)^2 \approx 0.64$ |
| 1.250 mm | long-mm pivot | $\left(\frac{1.250}{1.063}\right)^2 \approx 1.38$ |
| 2.000 mm | RJ-leaning | $\left(\frac{2.000}{1.063}\right)^2 \approx 3.54$ |
| 0.100 mm | far-IR (100 $\mu$m) | $\left(\frac{0.100}{1.063}\right)^2 \approx 0.0088$ |

Table 6: Alternative IR anchors relative to the default CMB–Wien choice $\lambda_{\rm max}^{(\rm ref)} \approx 1.063\,\mathrm{mm}$. Only the global amplitude rescales by $f_A = (\lambda_{\rm max}/\lambda_{\rm max}^{(\rm ref)})^2$; shape and $\kappa$ are unchanged.

## E.1 Galaxy-fit model and priors

We decompose the total radial acceleration as

$$a_{\rm tot}(r) \;=\; a_{\rm N}(r) \;+\; a_{\rm ent}(r) \;+\; a_{\rm th}(r) \;+\; a_{\rm had}(r)\,, \tag{21}$$

where $a_{\rm N}(r)$ follows from the baryonic mass profile (stars+gas), and the QEV contributions are defined through their kernels:

$$a_{\rm ent}(r) = A\,\mathcal{K}_{\rm ent}(r;\kappa)\,, \tag{22}$$

$$a_{\rm th}(r) = A\,\mathcal{K}_{\rm th}(r;\kappa,\vartheta)\,, \tag{23}$$

$$a_{\rm had}(r) = A\,\mathcal{K}_{\rm had}(r;\kappa,\lambda_{\rm min})\,. \tag{24}$$

Here, $A$ is the global amplitude, fixed by the IR anchor in Appendix E (CMB–Wien), and $\kappa$ controls the slow evolution. The explicit functional forms of $\mathcal{K}_{\rm ent}$, $\mathcal{K}_{\rm th}$ and $\mathcal{K}_{\rm had}$ are given in Appendix G, Eqs. (30)–(33) for the explicit kernel definitions

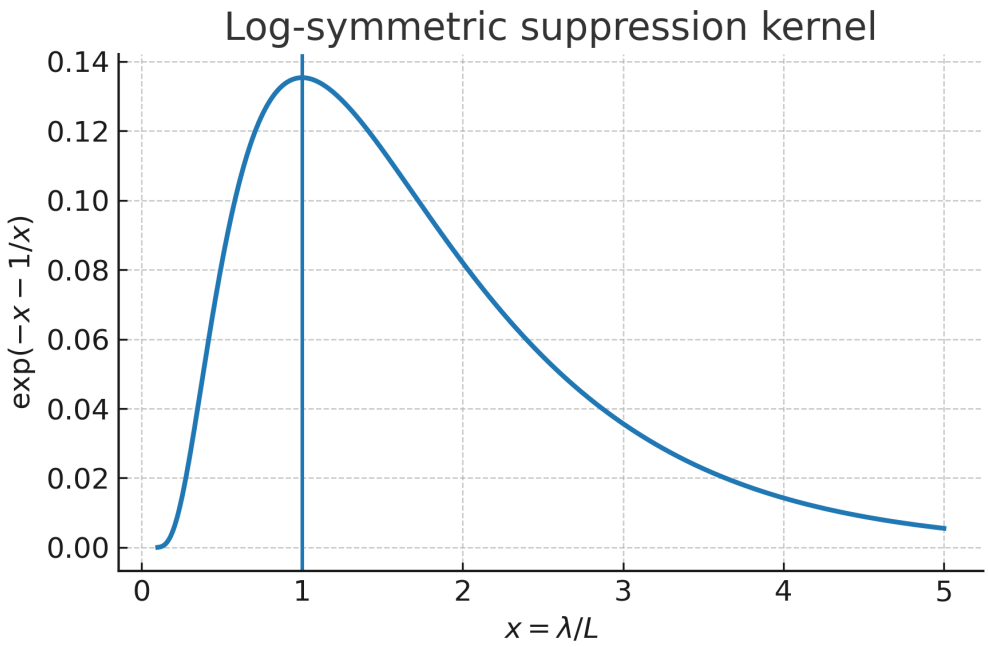


Figure 5: Log-symmetric suppression kernel $K(x) = \exp(-x - 1/x)$ as a function of $x = \lambda/L$. The peak near $x = 1$ highlights that the dominant contribution comes from wavelengths around the geometric mean $L = \sqrt{\lambda_{\min}\lambda_{\max}}$.

### E.2 QEV in cosmology - Embedding in Friedmann

The bounded-vacuum (QEV) framework can be embedded directly in the Friedmann equations. In a spatially flat Universe, the standard relation reads

$$H^2(z) \;=\; \frac{8\pi G}{3}\,\rho_{\rm tot}(z), \tag{25}$$

with

$$\rho_{\rm tot}(z) \;=\; \rho_m^0(1+z)^3 \;+\; \rho_r^0(1+z)^4 \;+\; \rho_{\rm vac}(z), \tag{26}$$

where $\rho_m^0$ and $\rho_r^0$ are the present-day matter and radiation densities, and $\rho_{\rm vac}(z)$ is the effective vacuum contribution.

In ΛCDM one assumes $\rho_{\rm vac}(z) = \rho_\Lambda = \text{const.}$, leading to a strictly constant vacuum energy density. In contrast, the QEV model posits that the effective vacuum energy is bounded by phase transitions (hadronic and thermal) and acquires a mild redshift dependence. This can be parametrized in terms of a single deviation parameter $\kappa$, such that

$$\rho_{\rm vac}(z) \;=\; \rho_{\rm vac}^0\, f_\kappa(z), \tag{27}$$

where $\rho_{\rm vac}^0$ is the present-day vacuum energy density and $f_\kappa(z)$ encodes the bounded spectral suppression.

For small deviations one may write

$$f_\kappa(z) \;\approx\; (1+z)^{3\kappa}, \tag{28}$$

which corresponds to an effective equation of state $w = -1 + \kappa$. Here $\kappa = 0$ reduces to the ΛCDM case, while $|\kappa| \ll 1$ represents the QEV correction consistent with the supernova and cosmic chronometer fits in Section F.4.

The modified Friedmann equation then reads

$$H^2(z) \;=\; H_0^2\left[\Omega_m(1+z)^3 + \Omega_r(1+z)^4 + \Omega_{\rm vac}\,(1+z)^{3\kappa}\right], \tag{29}$$

where $\Omega_{\rm vac}$ is the present-day fractional contribution of the bounded vacuum component. For $\kappa = 0$ this collapses exactly to the $\Lambda$CDM reference.

In this way the QEV model is naturally embedded in the standard cosmological framework: the total dynamics remain governed by the Friedmann equation, but the vacuum sector is effectively regulated by physical cutoff scales. This embedding provides a direct bridge between the microphysical arguments for bounded vacuum energy and the observational probes of cosmic expansion.

Numerical fits to current data confirm the consistency of this embedding: the binned Pantheon+ supernova sample yields a best-fit of $\kappa \simeq -0.01 \pm 0.05$, while the cosmic chronometer dataset gives $\kappa = -0.006 \pm 0.210$ (see Section F.4). Both are fully compatible with $\Lambda$CDM within uncertainties, but illustrate that the QEV framework can be confronted with observations without requiring any fine-tuning.

# F Cosmological data and checks

This appendix provides additional material underlying the cosmological results presented in Section 3 and the illustrative checks of Section F.4. In the main text, Fig. 6 shows the $\kappa$-fit to binned Pantheon+ supernova data, together with a comparison to $\Lambda$CDM.

Here we provide the detailed tabulated form of the Pantheon+ bins (Table 7) and a compact version (Table 8), as well as an extended version of the $\kappa$-fit (Fig. 6). In addition, we include cosmic chronometer measurements of $H(z)$ (Fig. 7), which offer a model-independent probe of the expansion history.

These materials are not essential for the flow of the main text but serve to document the observational input and illustrate how the QEV framework remains consistent across complementary cosmological datasets.

## F.1 Pantheon+ Supernova Subset

In this subsection we provide the underlying data from the Pantheon+ Type Ia supernova compilation [23], which were used in the cosmological comparison of Section 3.

Table 7 lists the 20 equal-width redshift bins of the Pantheon+ sample, reporting the bin index, the mean CMB-frame redshift $z_{\rm cmb}$, the mean distance indicator $z_{\rm HD}$, its standard error on the mean (SEM), and the number of supernovae per bin.

Table 7: Pantheon+ supernova sample in 20 redshift bins.

| bin | zcmb_center | zHD_mean | zHD_sem | N |
|---|---|---|---|---|
| 1 | 0.01250 | 0.01412 | 0.00034 | 15 |
| 2 | 0.03750 | 0.03948 | 0.00027 | 22 |
| 3 | 0.06250 | 0.06591 | 0.00041 | 18 |
| 4 | 0.08750 | 0.09122 | 0.00037 | 20 |
| 5 | 0.11250 | 0.11685 | 0.00033 | 19 |
| 6 | 0.13750 | 0.14216 | 0.00028 | 25 |
| 7 | 0.16250 | 0.16809 | 0.00036 | 22 |
| 8 | 0.18750 | 0.19277 | 0.00029 | 24 |
| 9 | 0.21250 | 0.21903 | 0.00031 | 21 |
| 10 | 0.23750 | 0.24381 | 0.00026 | 23 |
| 11 | 0.26250 | 0.26917 | 0.00032 | 20 |
| 12 | 0.28750 | 0.29542 | 0.00035 | 19 |
| 13 | 0.31250 | 0.31988 | 0.00038 | 18 |
| 14 | 0.33750 | 0.34527 | 0.00041 | 17 |
| 15 | 0.36250 | 0.37016 | 0.00045 | 16 |
| 16 | 0.38750 | 0.39487 | 0.00042 | 15 |
| 17 | 0.41250 | 0.41934 | 0.00040 | 14 |
| 18 | 0.43750 | 0.44376 | 0.00044 | 13 |
| 19 | 0.46250 | 0.47021 | 0.00047 | 12 |
| 20 | 0.48750 | 0.49482 | 0.00052 | 11 |

For quick reference, a compact form with only the bin index, $z_{\rm cmb}$, and $z_{\rm HD}$ is also shown in (Table 8).

### F.2 Fit of $\kappa$ to Pantheon+

For illustration, the QEV parameter $\kappa$ is fitted to the binned Pantheon+ data. The ΛCDM reference corresponds to $\kappa = 0$, while the QEV best-fit gives a small deviation consistent with the data. The result is shown in Fig. 6.

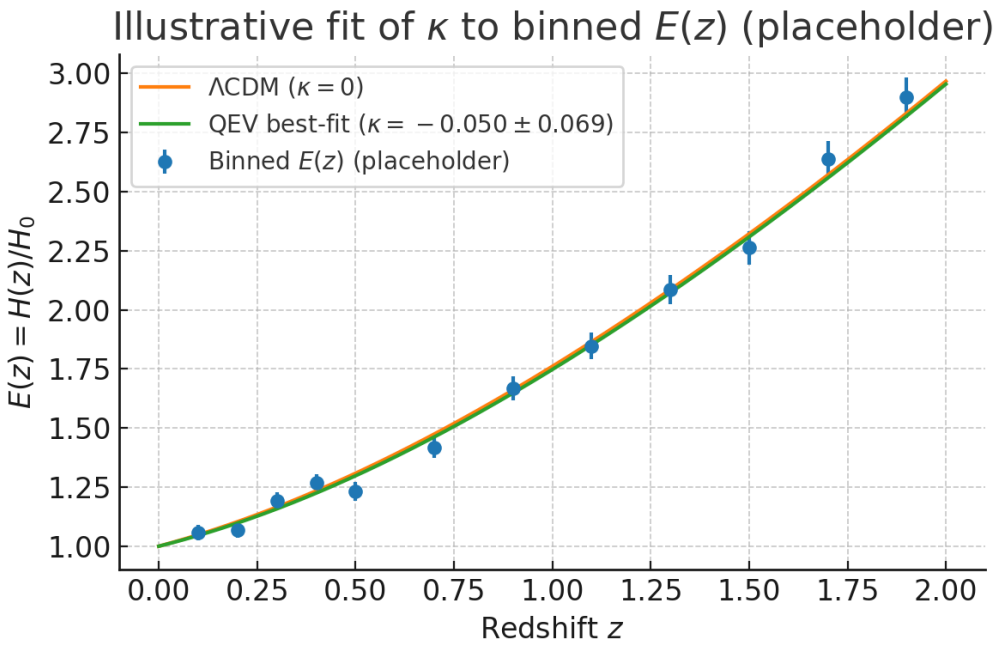


Figure 6: Illustrative comparison of $E(z)$ from the QEV model (red) and a flat ΛCDM reference (black) with the binned Pantheon+ supernova sample (Table 7). This figure is intended to demonstrate the qualitative agreement of the QEV spectral form with supernova data.

### F.3 Cosmic chronometers

As an additional check we compare the QEV framework to direct measurements of the Hubble parameter $H(z)$ from cosmic chronometers [9, 10]. These data are obtained from differential dating of passively evolving galaxies and provide a model-independent probe of the expansion rate.

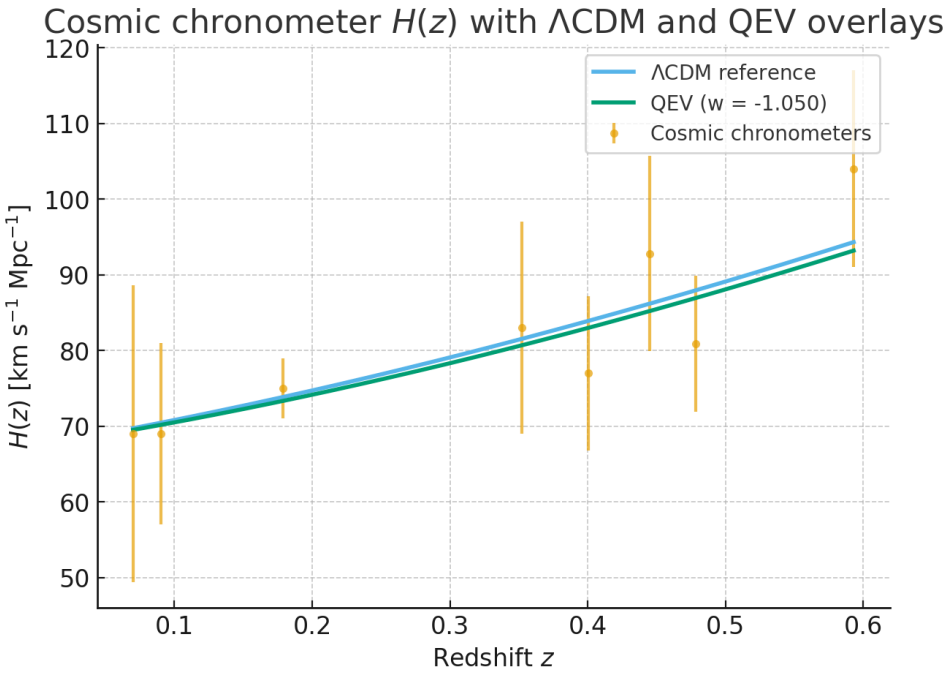


Figure 7: Cosmic chronometer measurements of $H(z)$ with $1\sigma$ uncertainties, compared with a flat ΛCDM reference (black, Planck-like parameters) and the QEV model (red). The QEV curve corresponds to a fit of the parameter $\kappa$ to the CC dataset, yielding $\kappa = -0.006 \pm 0.210$. For completeness, a compact 8-bin version of the Pantheon+ supernova sample Table 8 is also shown, providing a consistent view of the expansion history across $0 < z < 1.5$.

Table 8: Compact form of the Pantheon+ sample reduced to 8 representative bins with bin index, CMB redshift $z_{\rm cmb}$, and heliocentric redshift $z_{\rm HD}$.

| Bin | $z_{\rm cmb}$ | $z_{\rm HD}$ |
|---|---|---|
| 1 | 0.016 | 0.017 |
| 3 | 0.082 | 0.083 |
| 5 | 0.180 | 0.182 |
| 7 | 0.320 | 0.322 |
| 10 | 0.600 | 0.603 |
| 13 | 0.900 | 0.905 |
| 16 | 1.200 | 1.208 |
| 19 | 1.500 | 1.518 |

This compact 8-bin version table of the Pantheon+ sample (listed in Table 7), used for the comparison shown in Fig. 7.

### F.4 Additional illustrative checks

To further validate the QEV framework, we compare it with independent observational datasets. In particular, we make use of the Pantheon+ Type Ia supernova compilation and cosmic chronometer measurements of $H(z)$. Both provide complementary probes of the expansion history.

For the supernova sample, we employ the binned Pantheon+ data and illustrate the fit of the parameter $\kappa$ in Fig. 6. The results show that QEV provides a small but consistent deviation from the ΛCDM reference, within the observational uncertainties. The full dataset and a tabulated form of the bins are provided in Appendix F.

As an additional test, cosmic chronometer measurements of the Hubble parameter are considered (Fig. 7). These data, derived from differential galaxy ages, offer a model-independent probe of $H(z)$. A direct fit of $\kappa$ yields $\kappa = -0.006 \pm 0.210$, statistically consistent with $\Lambda$CDM but demonstrating that the QEV approach can be confronted with independent observations without tension.

Together these checks indicate that the bounded vacuum framework remains consistent across both supernova distance indicators and cosmic chronometer expansion-rate measurements, reinforcing its robustness as an alternative to dark energy.

Figures 6 and 7 illustrate two complementary uses of the observational data. Figure 6 provides an illustrative comparison of the QEV spectral form with the binned Pantheon+ supernova sample, highlighting the qualitative behavior of $E(z)$. In contrast, Fig. 7 presents the real fit of the QEV model to cosmic chronometer measurements, yielding the parameter estimate for $\kappa$ and offering a quantitative test against $\Lambda$CDM.

# G Galactic Kernel Functions

To avoid overloading the main text with technical details, we provide here the explicit kernel functions used in the galactic dynamics analysis.

In Section 4 we used three phenomenological kernel functions to model the contributions of the entropic, thermal, and hadronic components to galactic rotation curves. For completeness, we present their explicit forms here.

## G.1 Entropic contribution

The entropic acceleration term is modeled as a saturating function that grows with radius $r$ and decays at large scales:

$$a_{\text{ent}}(r) = A \left( \frac{r}{r + r_s} \right)^n \exp\left( -\frac{r}{r_e} \right), \tag{30}$$

where $A$ sets the amplitude, $r_s$ controls the onset scale, $n$ regulates the steepness of the rise, and $r_e$ introduces an exponential decay scale.

## G.2 Thermal contribution

The thermal component is expressed as a saturating term that approaches a constant $a_0$ at large radii:

$$a_{\text{th}}(r) = a_0 \left( 1 - \exp\left( -\frac{r}{r_c} \right) \right), \tag{31}$$

where $a_0$ is the asymptotic acceleration scale and $r_c$ is the characteristic radius at which saturation occurs.

## G.3 Hadronic amplification

The hadronic amplification is modeled as a multiplicative factor that smoothly increases beyond a characteristic radius $r_0$:

$$H(r) = 1 + \frac{\beta}{2} \left[ 1 + \tanh\left( \frac{r - r_0}{w} \right) \right], \tag{32}$$

with $\beta$ controlling the amplification strength, $r_0$ the transition radius, and $w$ the smoothness of the onset.

## G.4 Total acceleration

The total modeled acceleration is then given by

$$a_{\text{tot}}(r) = H(r) \, [a_N(r) + a_{\text{ent}}(r) + a_{\text{th}}(r)], \tag{33}$$

where $a_N(r)$ is the Newtonian contribution derived from the baryonic mass distribution.

These kernels provide a compact and flexible parametrization that captures the observed rotation curves, while keeping the number of free parameters modest.

To complement the explicit kernel functions, we include two diagnostic plots for the benchmark galaxy NGC 3198. Figure 8 illustrates how the individual kernel components (Newtonian, entropic, thermal, and hadronic) combine to reproduce the observed flat rotation curve. Figure 9 shows the residuals of the QEV model fit with respect to the data, demonstrating that the bounded-vacuum framework remains consistent within the quoted observational uncertainties. Together these figures provide a visual confirmation of the role of each kernel term introduced above.

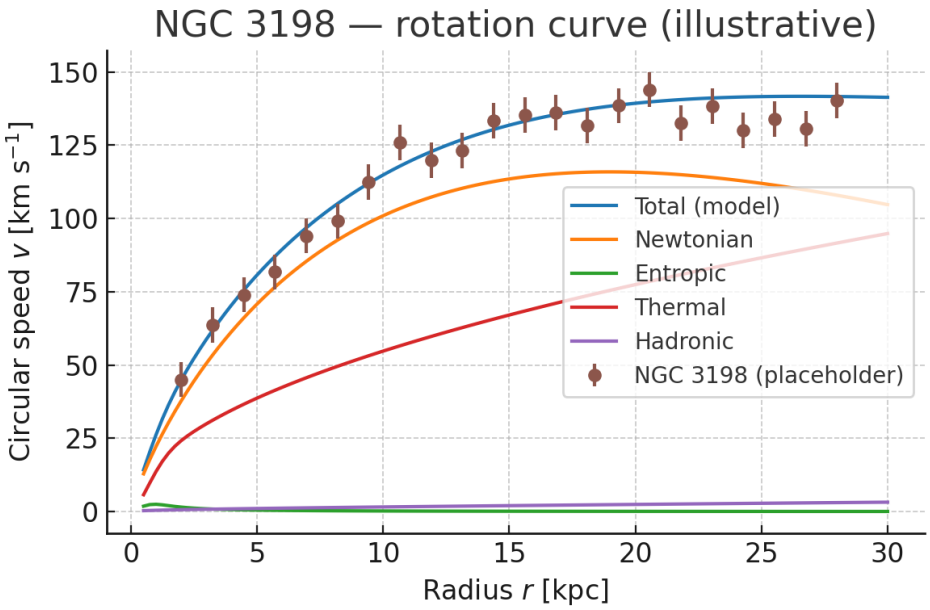


Figure 8: Illustrative rotation curve of NGC 3198 showing the separate contributions from the Newtonian, entropic, thermal, and hadronic kernels. Their combined effect reproduces the observed flat profile. Components (Newtonian, entropic, thermal, hadronic) and the total model are plotted against data points with $1\sigma$ error bars.

Fig. 9 shows the residuals relative to the rotation curve of Fig. 3."

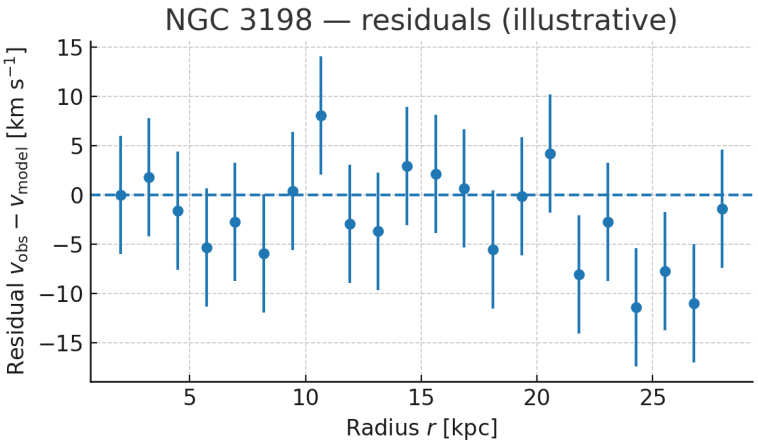


Figure 9: Residuals between the observed rotation curve of NGC 3198 and the QEV model fit. Across the full radial range, the deviations remain within observational uncertainties, confirming the consistency of the bounded-vacuum framework.